Solar steam generation enabled by carbon black
The impact of particle size and nanostructure

Kelesidis, Georgios A.; Nagarkar, Amogh; Rivano, Pier Giuseppe

DOI
10.1002/aic.18619

Publication date
2024

Document Version
Final published version

Published in
AIChE Journal

Citation (APA)
Kelesidis, G. A., Nagarkar, A., & Rivano, P. G. (2024). Solar steam generation enabled by carbon black: The impact of particle size and nanostructure. *AIChE Journal*, *70*(12), Article e18619. https://doi.org/10.1002/aic.18619

Received: 16 May 2024 | Revised: 20 August 2024 | Accepted: 17 September 2024

DOI: 10.1002/aic.18619

RESEARCH ARTICLE

Particle Technology and Fluidization

AIChE JOURNAL

Solar steam generation enabled by carbon black: The impact of particle size and nanostructure

Georgios A. Kelesidis[1,2] | Amogh Nagarkar[2] | Pier Giuseppe Rivano[2]

[1]Faculty of Aerospace Engineering, Delft University of Technology, Delft, The Netherlands

[2]Particle Technology Laboratory, Institute of Energy and Process Engineering, Department of Mechanical and Process Engineering, ETH Zürich, Zürich, Switzerland

Correspondence
Georgios A. Kelesidis, Faculty of Aerospace Engineering, Delft University of Technology, Kluyverweg 1, 2629 HS Delft, The Netherlands.
Email: g.kelesidis@tudelft.nl

Funding information
Schweizerischer Nationalfonds zur Förderung der Wissenschaftlichen Forschung, Grant/Award Numbers: 200020_182668, 206021_170729, 250320_163243; ETH Zürich Foundation; Particle Technology Laboratory

Abstract

Here, commercial carbon black (CB) grades are characterized in detail to determine the link between their physicochemical properties and solar steam generation performance. The CB nanoparticles used here have surface mean primary particle diameters of 11–406 nm resulting in specific surface areas of 8–300 m^2/g. Thermogravimetric analysis, dynamic light scattering, Raman spectroscopy, and x-ray diffraction reveal that fine CB nanoparticles form large agglomerates, have a more disordered nanostructure and larger organic carbon content than coarse CB grades. Most importantly, UV–vis spectroscopy and Mie theory show that increasing the particle size from 14 to 406 nm reduces the light absorption of CB dispersed in water up to 86%. So, the water evaporation flux of suspensions containing 11–14 nm CB nanoparticles is up to 25% larger than that obtained for suspensions of 406 nm particles. Thus, good control of particle size is essential to optimize the solar steam generation enabled by CB.

KEYWORDS
carbon black, light absorption, nanostructure, particle size, solar steam generation

1 | INTRODUCTION

Steam production is essential for a wide range of applications, including large-scale electricity generation,[1] water desalination and purification,[2] as well as sterilization of medical instruments.[3] Steam is commonly generated using methods that are burdensome for the environment, such as fossil fuel combustion or direct heating from electricity.[4] To this end, solar light, an abundant, clean, and renewable energy source, has attracted significant interest for steam generation.[5] Solar steam generation has been identified as a promising solution to address the rising global electricity consumption with a green energy source,[4] as well as the drinking water scarcity[6] that affects nearly 2.5 billion people globally. Solar desalination has emerged as the most straightforward way to produce fresh water with small environmental impact.[7] However, low cost-effectiveness and energy efficiency have constrained its large-scale deployment.[8] Likewise, large energy requirements have also limited the adoption of steam-based autoclave systems for medical sterilization.[3] In this regard, the use of light absorbing nanoparticles for steam generation has increased the potential of this process,[3] especially in developing countries where healthcare-associated infections due to exposure to unsanitary equipment are a long-standing problem.[9]

During bulk or volumetric steam generation, light absorbing nanoparticles are dispersed in water and exposed to solar light.[3] The energy absorbed by the dispersed nanoparticles is dissipated in the surrounding water molecules via thermal diffusion.[5] This results in bulk water boiling, as well as non-equilibrium steam generation near the particle surface.[3] The potential of volumetric solar steam generation has been explored using plasmonic[4] and carbonaceous nanomaterials.[10] Specifically, gold nanoparticles have been used for solar steam generation due to their surface plasmon resonance exhibited in the visible light range (~530 nm).[11] The water evaporation rate increases with increasing gold mass

concentrations, C, and levels off at C >180 ppm.[12] The high cost of gold limits its use in large-scale applications of solar steam generation. So, carbon black (CB) is quite attractive due to its strong light absorption over the entire solar spectrum[10] and low cost.[13] Water containing carbonaceous nanoparticles evaporates at 40–70% larger rates compared to water containing gold nanoparticles.[14] Furthermore, the cost for steam production at a rate of 1 g/s using gold is 300 times higher than that obtained using CB.[14] This highlights the large potential of carbonaceous nanomaterials for solar steam generation.

The link between the solar steam generation by CB and its physicochemical properties has not been determined yet. The agglomerate and primary particle diameter, d_p, specific surface area, *SSA*, and nanostructure vary between different CB grades and depend on the combustion conditions used for their synthesis.[15] During incomplete combustion of gaseous or liquid hydrocarbon fuels, CB nanoparticles are incepted and grow by surface reactions and coagulation to form agglomerates.[16] Increasing the fuel flow rate or reducing the temperature increases the CB d_p and decreases its *SSA*.[17] So, CB nanoparticles produced by the furnace process can have small d_p and large *SSA*, while CB grades generated by the lamp or thermal processes contain large nanoparticles with small *SSA*.[18] The CB nanoparticles have a rather turbostratic structure and lack the stack periodicity of the graphene basal planes of graphite.[19] The CB nanostructure is commonly characterized by the intensity ratio of the Raman D and G bands,[20] as well as the interlayer spacing, d, and crystallite length, L_c, of their constituent graphene basal planes.[21] The volatile and semi-volatile polycyclic aromatic hydrocarbons adsorbed on the CB surface are quantified by the organic carbon (OC) content.[22] The combustion conditions determine the nanostructure and OC content of CB.[22] For example, carbonaceous nanoparticles emitted from jet fuel combustion can have $D/G = 0.84–0.96$[23] and 10–40 wt% OC content[24] depending on the oxygen flow rate. The particle size,[25] OC content[26] and nanostructure[27] affect the light absorption of carbonaceous nanoparticles and thus their solar steam generation.

Despite the availability of CB grades with a wide range of particle sizes and nanostructures, only a few have been used so far for solar steam generation. In particular, CB nanoparticles with $d_p = 15–42$ nm produced using the furnace process have been dispersed in water[10,14,28] or deposited on membranes[29] to improve steam production. The largest water evaporation flux has been obtained for Vulcan CB with $d_p = 15$ nm at $C = 5000$ ppm.[10] Thus, it is essential to elucidate the impact of the particle size and nanostructure on the solar steam generation using CB. This would enable the optimization of CB grades for large-scale electricity generation,[1] water desalination and purification,[2] as well as sterilization of medical instruments.[3]

Here, commercial CB grades are characterized in detail to determine the optimal physicochemical properties for solar steam generation. The CB d_p, *SSA*, hydrodynamic diameter, OC content and nanostructure are quantified by N_2 adsorption, microscopy imaging, dynamic light scattering, thermogravimetric analysis, Raman spectroscopy and x-ray diffraction. The light absorption of CB is measured by UV–Vis spectroscopy and estimated using the Mie theory and discrete dipole approximation. Most importantly, the water evaporation flux is obtained for various CB grades at $C = 5–3000$ ppm using a solar simulator. That way, the impact of various material properties on the CB light absorption and solar steam generation is elucidated, for the first time to the best of our knowledge.

2 | MATERIALS AND METHODS

2.1 | Physicochemical characterization of commercial CB grades

The commercial CB grades of Color Black, Printex 95, Printex U, Printex G, Lamp Black, and Arosphere (Orion Engineered Carbons) were used here to explore a wide range of CB particle sizes, organic carbon (OC) contents and nanostructures. The number-based mean primary particle diameter, d_p, and specific surface area, *SSA*, of all CB grades were provided by the manufacturer.[30] High magnification transmission electron microscopy images were acquired from the commercial CB grades on a Tecnai F30 microscope (FEI) operated at 300 kV. The CB *SSA* was analyzed by N_2 adsorption on a Tristar II Plus surface area and porosity system (Micromeritics) at 77.3 K after degassing in vacuum (VacPrep 061, Micromeritics) at 200°C overnight. The CB *SSA* was obtained for relative pressures between 0.05 and 0.25. This is consistent with the relative pressure range of 0.05–0.30 recommended for organic nanomaterials.[31] Based on the *SSA* measured from N_2 adsorption and the CB bulk density, $\rho = 1.8$ g/cm^3, the surface mean primary particle diameter, d_{va}, was estimated by[32]:

$$d_{va} = 6/(SSA \cdot \rho). \quad (1)$$

The x-ray diffraction (XRD) patterns of CB grades at diffraction angles, $2\theta = 10°–70°$ were obtained using an AXS D8 diffractometer (Bruker) at a scan rate of 0.0197°/s. Here, the mean d of CB was obtained by analyzing the 002 XRD peak using Bragg's law[21]:

$$d = \frac{n \cdot \lambda}{2 \sin \theta_{002}}, \quad (2)$$

where $n = 1$ is the order of diffraction, $\lambda = 0.154$ nm is the wavelength of the diffractometer, and θ_{002} is the angle of the 002 peak. Similarly, the mean L_c of CB was obtained by[21]:

$$L_c = \frac{K \cdot \lambda}{\beta_{002} \cos \theta_{002}}, \quad (3)$$

where $K = 0.89$ is the peak shape factor[21] and β_{002} is the full width of the half maximum of the 002 peak. The crystallite d and L_c were determined here using Equations (2) and (3) with the θ_{002} and β_{002} derived from the measured XRD patterns. In specific, the CB θ_{002} and β_{002} were obtained by fitting a Gaussian distribution to the measured 002 peak.[33]

Raman spectra of CB nanoparticles were obtained using a 515 nm laser having 50 mW power (Renshaw inVia). The laser was

focused with a × 20 magnification optical microscope, which gives a 2 μm spot size, while a 10% laser power was focused on the sample for 120 s and three acquisitions.[34] The intensities of the disorder (D ~1350 cm^{-1}) and graphitic (G ~1580 cm^{-1}) bands[34] were obtained after straight line subtraction of the baseline.[35] The mean length of the graphene basal plane, L_a, was derived based on the measured D/G ratio and the energy of the incident photon, $E_L = 2.41$ eV[36]:

$$L_a{}^2 = 5.4 \times 10^{-2} \times E_L{}^4 \times (D/G). \quad (4)$$

The organic to total carbon (OC/TC) mass ratio of CB was obtained by thermogravimetric analysis (TGA).[37] The samples were first placed in N_2 to volatilize OC and then in air to oxidize the non-volatile CB. The sample heating began at 30°C in N_2 and was ramped up to 900°C at 20°C/min. The temperature was held at 900°C for 10 min before dropping back to 30°C at 20°C/min. The same temperature profile was then repeated in air. From the TGA mass loss, the OC/TC was estimated as the ratio of mass lost under N_2 divided by the total mass lost in both stages.

2.2 | Measurement and estimation of CB light absorption in water

Aqueous suspensions of CB nanoparticles were prepared by dispersing CB in 100 mL of milli-Q water. The CB mass concentration, C, was varied from 5 to 3000 ppm by increasing the dispersed CB mass from 5 to 60 mg. All aqueous suspensions were sonicated at an intensity of 100 kJ/L for 3–5 min to prevent agglomeration of CB particles. The number-based distribution of the CB hydrodynamic diameter, d_h (Figure S1), was measured by dynamic light scattering (DLS) using a Zetasizer (Nano ZS, Malvern Instruments) for suspensions with $C = 50$ ppm. It should be noted that Lamp Black could not be characterized by the DLS instrument used here. The mean number of primary particles per agglomerate, n_p, was derived based on a power law for agglomerates of polydisperse primary particles with a geometric mean diameter, d_{pg}, and a standard deviation, $\sigma_{gp} = 1.2$[38]:

$$n_p = 1.18(d_h/d_{pg})^{1.92}. \quad (5)$$

The light absorption of dispersed CB nanoparticles at wavelengths, $\lambda = 350$–800 nm was measured using a UV–Vis spectrophotometer (Cary Varian 500).

The light absorption of CB spheres with $d_p = 14$, 40, 80, 160 and 400 nm dispersed in water or suspended in air was also estimated using the Mie theory.[39] The refractive index, RI, derived for carbonaceous nanoparticles with OC/TC = 0% from diffusion propane flames for $\lambda = 300$–800 nm[40] was used. In order to elucidate the impact of the CB nanostructure on its light absorption, a recent RI relation[26] that accounts for the nanostructural changes of CB was also used for spheres with $d_p = 40$ nm and OC/TC = 0–8%.

In addition to Mie theory for spheres, discrete dipole approximation (DDA) was used to estimate the CB light absorption accounting for its realistic agglomerate structure. The light absorption[41] and scattering[42] derived by DDA have been described in detail[27] and validated with experimental data for soot[43] and gold[44] nanoparticle agglomerates. In brief, discrete element modeling (DEM) for coagulation at 1 atm and 1830 K[16] was used to generate simulated agglomerates of polydisperse primary particles with geometric mean $d_{pg} = 40$ nm and $\sigma_{gp} = 1.2$. The latter is consistent with primary particle size distributions measured commonly for carbonaceous nanomaterials.[17,42,45] So, DDA calculations were done using the open-source DDSCAT 7.3 code[46] for DEM-derived CB agglomerates with $n_p = 1$, 17, 34, and 51. The fractal-like agglomerate morphology is represented on a lattice by an array of discrete dipoles interacting with each other through their electric fields.[46] The Maxwell's equations are discretized on the lattice using the volume-integral equation method and solved iteratively.[46] The dipole spacing, s, must be small compared to the incident light wavelength, λ, to calculate accurately the CB absorption efficiency, Q_{abs}.[46] For accurate but also efficient DDA computations, s is varied for different λ and CB RI to have a ratio $2\pi|RI|s/\lambda < 0.12$, satisfying the precision criteria[47] for strongly absorbing materials, such as CB. The CB mass absorption cross-section, MAC, was obtained based on Q_{abs} derived by Mie theory and DDA[27]:

$$MAC = 3Q_{abs}/(2d_v \cdot \rho), \quad (6)$$

where d_v is the volume-equivalent diameter of agglomerates, while for spheres $d_v = d_p = d_{va}$.

2.3 | Solar steam generation by carbon black nanoparticles

Cylindrical glass beakers (diameter: 1.9 cm, height: 4.7 cm) containing aqueous suspensions of CB nanoparticles were exposed to solar light at an intensity of 100 mW/cm^2 (1 sun) for 24 h using a solar simulator (SolarSim150, Solaronix). During the solar light illumination, the CB suspensions were continuously stirred using a cylindrical magnetic stirrer to prevent particle settling.

The CB suspension weight was measured before (m_o) and after 24 h of solar light illumination (m_f) using an electronic scale (Mettler Toledo AB135-S) with a precision of 0.1 mg. So, the water evaporation flux, F, from CB suspensions was derived by:

$$F = (m_f - m_o)/(t\,a), \quad (7)$$

where $t = 24$ h is the solar illumination period and $a = 2.83$ cm^2 is the open surface area of the beaker. The evaporation flux enhancement, E (%), was estimated based on F and the evaporation flux, F_w, of pure milli-Q water in the absence of CB:

$$E = 100\,(F - F_w)/F_w. \quad (8)$$

3 | RESULTS AND DISCUSSION

3.1 | CB size, surface area, and composition

Figure 1 shows high magnification microscopy images of Color Black (A), Printex 95 (B), Printex U (C), Printex G (D), Lamp Black (E), and Arosphere (F) along with their number-based mean particle diameter, d_p provided by the manufacturer.[30] Color Black, Printex 95, Printex U, and Printex G contain rather fine CB primary particles with d_p ranging from 13 (Color Black) to 51 nm (Printex G). The mean d_p of gas and furnace CB grades can be varied by close control of the fuel flow rate and furnace temperature.[17] The coarse grades of Lamp Black and Arosphere are produced by the lamp and thermal black processes, respectively, resulting in $d_p = 95$ and 280 nm, respectively. The CB nanoparticles produced by gas, furnace or lamp black processes are connected with each other through chemical bonding (necking) formed by surface growth and aggregation.[45] In contrast, the large, spherical Arosphere particles are either single or connected with each other by physical bonding (point contacts). This indicates that surface growth is dominant during the thermal black process, while aggregation is rather limited.

Table 1 shows the specific surface area, *SSA*, surface mean particle diameter, d_{va}, organic to total carbon (OC/TC) mass ratio, mean hydrodynamic diameter, d_h, number of primary particles per agglomerate, n_p, crystallite size, L_c, and graphene basal plane length, L_a, measured for the CB grades shown in Figure 1. The CB *SSA* measured

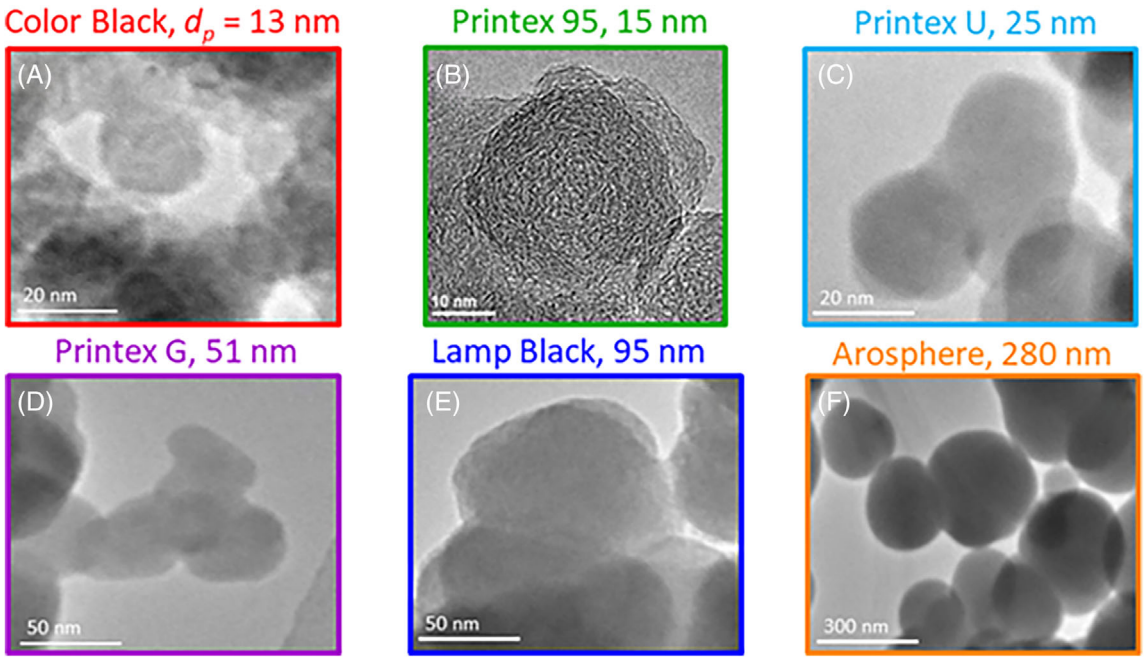

FIGURE 1 High magnification microscopy images of Color Black (A), Printex 95 (adapted from ref)[50] (B), Printex U (C), Printex G (D), Lamb Black (E), and Arosphere (F) along with their mean primary particle diameter, d_p, provided by the manufacturer[30] (Orion Engineered Carbons).

TABLE 1 Specific surface area, *SSA*, surface mean particle diameter, d_{va}, organic to total carbon (OC/TC) mass ratio, mean hydrodynamic diameter, d_h, number of primary particles per agglomerate, n_p, crystallite size, L_c, and graphene basal plane length, L_a, of all CB grades measured here along with the *SSA* provided by the manufacturer.[30]

CB grade	Specific surface area, *SSA*, m^2/g		Surface mean particle diameter, d_{va}, nm	Organic to total carbon mass ratio, OC/TC	Mean hydrodynamic diameter, d_h, nm	Mean number of primary particles, n_p	Mean crystallite size, L_c, nm	Mean graphene basal plane length, L_a, nm
	Manufacturer[30]	This work						
Color Black	320	296	11.2	8.5	145.7 ± 9.4	190.8	1.3	1.34
Printex 95	250	236	14.1	3.2	90.1 ± 1.8	48.7	1.5	1.32
Printex U	92	88	37.8	6.7	155 ± 3	20.8	1.1	1.21
Printex G	35	44	76.6	0.3	255.2 ± 5.2	14	1.8	1.26
Lamp Black	29	21	156.5	0.6	–	–	1.2	1.26
Arosphere	9	8	406.5	0.1	407 ± 16	1.4	1.8	1.27

here are in good agreement with those given by the manufacturer,[30] as well as those obtained previously for Printex U (96 m^2/g) and Printex G (45 m^2/g).[48] This validates the present N_2 adsorption measurements. As shown in Figure 1, all CB nanoparticles investigated here have negligible internal porosity. So, the particle surface area is determined by its d_p with fine CB grades having larger *SSA* than coarser ones. The d_{va} derived based on the *SSA* measured for Printex U, Printex G, Lamp Black, and Arosphere is larger than the number based mean d_p (Figure 1). This difference can be attributed to the necking between CB primary particles that decreases the *SSA* and shifts the surface mean d_{va} to larger sizes.[32] So, the optical properties of CB should be determined based on the d_{va} rather than the number-based mean d_p to account for the realistic CB surface area that interacts with solar light (Figure 5). Most CB nanoparticles investigated here form agglomerates with large d_h and n_p. The CB n_p decreases from 190.8 to 1.4 with increasing d_{va}.

Volatile and semi-volatile organic species (i.e., organic carbon) adsorb on the surface of carbonaceous nanoparticles during combustion synthesis, reducing their light absorption[26] and thus their steam generation rate. Fine CB grades (i.e., Color Black, Printex 95, and Printex U) have larger OC/TC compared to those measured for coarse grades. This is consistent with thermogravimetric and thermo-optical analysis of carbonaceous nanoparticles from propane[49] and jet fuel[24] combustion showing that OC/TC decreases with increasing particle diameter.

3.2 | Characterization of CB nanostructure

The CB nanostructure is quantified here by x-ray diffraction (XRD) and Raman spectroscopy. Figure 2 shows the XRD patterns along with the mean interlayer distance, d, and crystallite length, L_c, of the CB grades shown in Figure 1. The XRD pattern of Printex 95 exhibits a rather broad 002 peak (broken line) at a diffraction angle, 2θ, of about 24° that yields $d = 3.7$ Å and $L_c = 1.5$ nm, in agreement with previous XRD analysis of the same CB grade.[50] Color Black nanoparticles have also $d = 3.7$ Å, while CB grades containing larger nanoparticles than Color Black and Printex 95 exhibit $d = 3.6$ Å. The CB L_c varies from 1.1 (Printex U) to 1.8 nm (Printex G and Arosphere). The CB L_c measured here are in good agreement with those obtained previously for Printex U (1.1 nm) and Printex G (1.9 nm).[48] This validates the present XRD analysis.

Figure 3 shows the Raman spectra along with the mean ratio of the disorder (*D*) over the graphitic (*G*) band intensity of the CB grades shown in Figure 2. The *D*/*G* ratio is often used to quantify the disorder of the CB nanostructure.[51] The largest degree of disorder is obtained for Color Black and Printex 95 (0.95–0.98), while Printex U has the smallest $D/G = 0.81$ among the CB grades characterized here. The $D/G = 0.81$–0.98 measured here for different CB grades is consistent with those measured for carbonaceous nanoparticles produced from jet fuel combustion.[23] The mean graphene basal plane length, L_a, of CB increases with increasing *D*/*G*.[36] So, the fine CB grades (Color Black, Printex 95) have $L_a = 1.32$–1.34 nm, while coarse CB grades (Lamp Black, Arosphere) have $L_a = 1.26$–1.27 nm. The CB L_a measured here are within the L_a range measured for flame-made carbonaceous nanoparticles.[52]

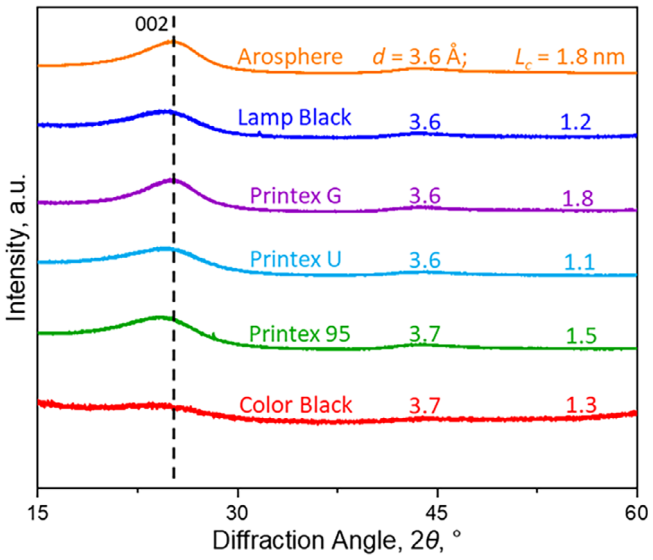

FIGURE 2 X-ray diffraction patterns of Color Black (red line), Printex 95 (green line), Printex U (light blue), Printex G (purple line), Lamb Black (blue line), and Arosphere (orange line) along with their interlayer distance, *d*, and crystallite length, L_c, obtained based on the 002 peak (broken line).

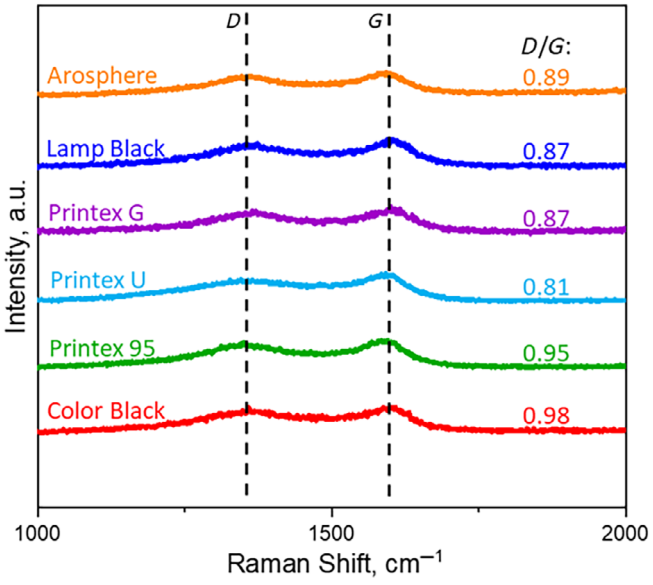

FIGURE 3 Raman spectra of Color Black (red line), Printex 95 (green line), Printex U (light blue), Printex G (purple line), Lamb Black (blue line), and Arosphere (orange line) along with the ratio of their D and G band intensities (broken lines).

Based on the CB *d* and *D*/*G* measured by XRD (Figure 2) and Raman spectroscopy (Figure 3), Color Black and Printex 95 nanoparticles are rather amorphous and have a disordered nanostructure. So, Printex U, Printex G, Lamp Black, and Arosphere contain less disordered nanoparticles than the fine Color Black and Printex 95 grades.

This increase of graphitization with increasing particle size is in line with Raman and XRD analysis of carbonaceous nanoparticles from methane[53] and jet fuel combustion[23] and may enhance the light absorption of CB nanoparticles.[27]

3.3 | Light absorption of CB nanoparticles

Figure 4 shows the UV–Vis spectra of Color Black (dotted line), Printex 95 (thin solid line), Printex U (dot broken blue), Printex G (double dot broken line), Lamb Black (broken line), and Arosphere (solid line) dispersed in water at a concentration, $C = 50$ ppm. The light absorption of CB nanoparticles produced by the furnace process (i.e., Color Black, Printex 95, Printex U, and Printex G) decreases with increasing wavelength, λ, according to a power law,[26] consistent with measurements of CB light absorption in air.[54] In contrast, the light absorption of coarse Lamp Black and Arosphere nanoparticles produced by the lamp and thermal black processes, respectively, does not vary with λ. Most importantly, the light absorption of CB nanoparticles seems to increase with decreasing d_{va}. In particular, Color Black and Printex 95 exhibit the highest light absorption in water solutions despite having larger amorphous (Figures 2 and 3) and organic carbon (Table 1) content compared to the other CB grades. So, the particle size seems to determine the light absorption of CB dispersed in water.

In order to corroborate the impact of the particle size on the light absorption of CB, the mass absorption cross-section, *MAC*, was estimated for spheres with $d_p = d_{va} = 14$–400 nm using the Mie theory (Figure 5). The d_p range used in Mie theory covers the range of the CB d_{va} measured here (Table 1). The impact of particle size on CB light absorption was determined here for non-porous nanoparticles. So, the connection between particle size and *MAC* might be different for oxidized CB grades containing tiny pores with large surface area.[50] The *MAC* of CB particles with $d_p = 14$ nm decreases with λ, in line with the UV–vis spectra of Color Black and Printex 95 that have similar d_{va}. Increasing d_p from 14 to 40 nm does not affect significantly the estimated CB *MAC*. This explains, to some extent, the UV–vis spectrum of Printex U that is similar to those of Color Black and Printex 95. Further increasing d_p up to 400 nm reduces *MAC* up to 86% and weakens its variability with λ. So, the small *MAC* derived for $d_p = 400$ nm is consistent with the UV–vis spectrum measured for Arosphere CB with similar d_{va}. These Mie theory calculations corroborate the large impact of the particle size on CB light absorption. In this regard, the CB *MAC* decreases with increasing d_p regardless of the medium. However, this reduction is less pronounced for CB suspended in air (Figure S2).

The OC/TC of the CB grades investigated here varies from 0 to about 8% (Table 1). Increasing the OC/TC from 0 (Figure 6A: dot-broken line) to 4 (solid line) or 8% (broken line) reduces *MAC* of CB up to 14%. This confirms that the variations of the CB nanostructure and OC content do not alter significantly its light absorption. It should be noted that the CB agglomerate morphology is neglected by Mie theory. So, Figure 6B shows the CB *MAC* as a function of λ derived by discrete dipole approximation for agglomerates with $n_p = 1$ (dot-broken line), 17 (broken line), 34 (dotted line) and 51 (solid line). Agglomerates of CB nanoparticles absorb up to 30% less light compared to single spheres at $\lambda = 300$ nm. At $\lambda \geq 500$ nm though, the agglomerate *MAC* is practically identical with that of spheres. Increasing the agglomerate n_p from 17 to 51 barely affects the CB *MAC*. This further confirms that d_p rather than n_p determines the CB light absorption.

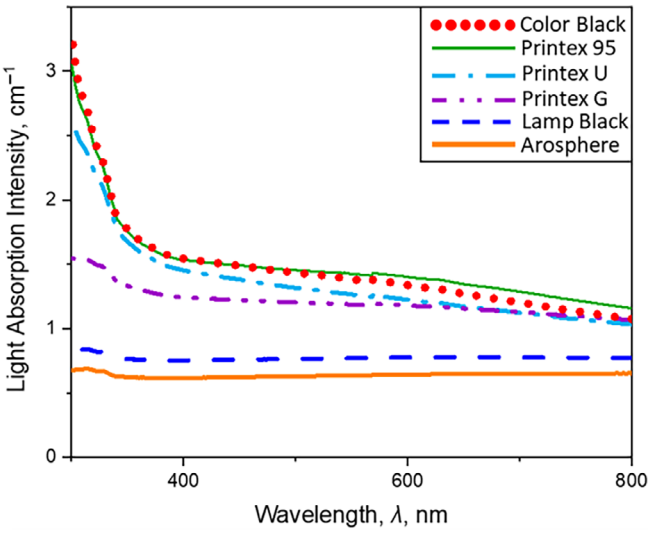

FIGURE 4 Light absorption intensity measured as a function of wavelength, λ, for Color Black (dotted line), Printex 95 (thin solid line), Printex U (dot broken blue), Printex G (double dot broken line), Lamb Black (broken line), and Arosphere (solid line) dispersed in water at a concentration, $C = 50$ ppm.

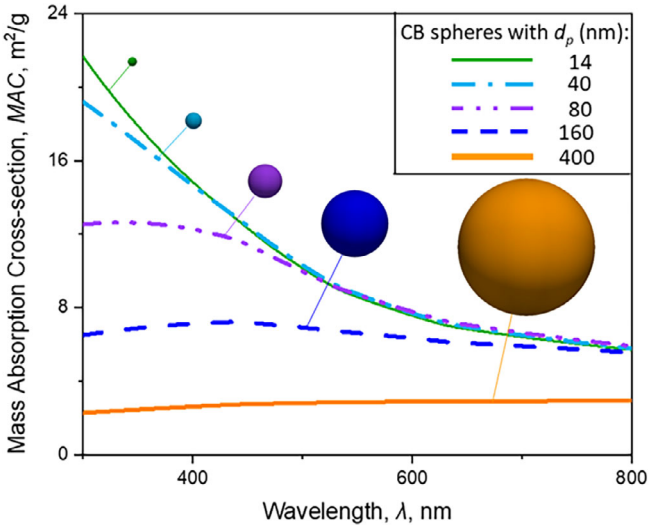

FIGURE 5 Mass absorption cross-section, *MAC*, derived as a function of λ for spheres with $d_p = 14$ (thin solid line), 40 (dot-broken line), 80 (double dot-broken line), 160 (broken line), and 400 nm (solid line).

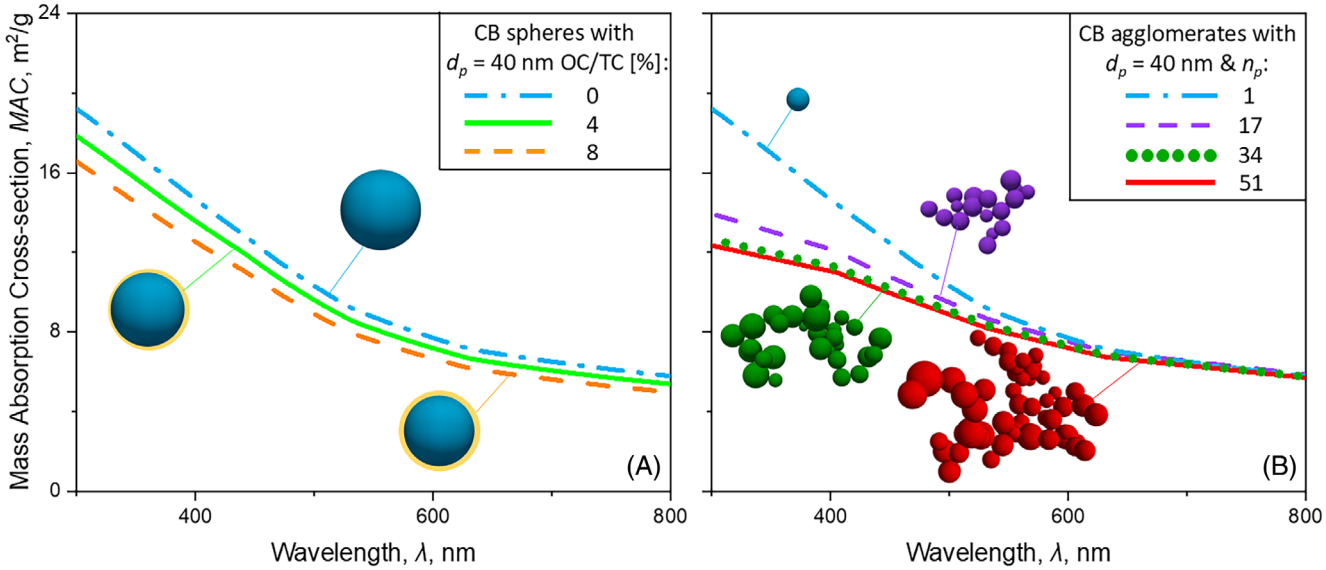

FIGURE 6 (A) The *MAC* derived as a function of λ for spheres with $d_p = 40$ nm and OC/TC = 0 (dot-broken line), 4 (solid line), and 8% (broken line). (B) The *MAC* as a function of λ derived by discrete dipole approximation for CB agglomerates with $d_p = 40$ nm and number of primary particles, $n_p = 1$ (dot-broken line), 17 (broken line), 34 (dotted line), and 51 (solid line).

3.4 | Solar steam generation by CB nanoparticles

Figure 7 shows the water evaporation flux enhancement, *E* measured as a function of CB mass concentration in water, *C*, for Color Black (squares), Printex 95 (triangles) and Arosphere (diamonds). The CB *E* was obtained based on Equation (8) using the evaporation flux, *F*, measured for water with and without CB nanoparticles (Figure S3). The CB grades were selected based on their d_{va} and UV–vis spectra. Color Black and Printex 95 particles have similar d_{va} and light absorption, while Arosphere particles have the largest d_{va} and lowest light absorption among all CB grades investigated here.

The presence of CB nanoparticles even at small $C = 5$ ppm enhances the water evaporation flux by about 5–16%. This is attributed to the strong light absorption of CB in the entire solar spectrum. As *C* increases up to about 3000 ppm, the water evaporation flux increases up to about 75%. Among all CB grades used here, Arosphere exhibits the smallest water evaporation flux. This can be attributed to the small light absorption by Arosphere particles compared to the other CB grades (Figure 4). As the CB d_{va} decreases from 406 (Arosphere) to 14 (Printex 95) or 11 nm (Color Black), the water evaporation flux is enhanced up to about 25%. So, the particle size seems to determine the solar steam generation by CB dispersed in water. In this regard, the water evaporation flux of about 3.3×10^{-2} mg/(s·cm^2) measured here for Color Black and Printex 95 at $C = 500$–3000 ppm is in line with that obtained at $C = 5000$ pm using a CB grade with similar d_{va} adjusted for the same light intensity.[10] This validates the present water evaporation flux measurements and indicates that large steam production rates can be obtained even at small *C*.

It should be noted that all aqueous suspensions of CB are sonicated during illumination with solar light to avoid particle sedimentation. However, in the absence of sonication, Arosphere particles with large mean $d_h = 407$ nm (Figure S1: solid line) settle faster than Printex 95 (thin solid line) and Color Black (dotted line) that have 80 and 65% smaller d_h, respectively. This may further limit the solar steam generation rate induced by Arosphere. In this regard, increasing the CB concentration may enhance the coagulation of Arosphere particles and their d_h,[16] reducing their performance in solar steam generation.

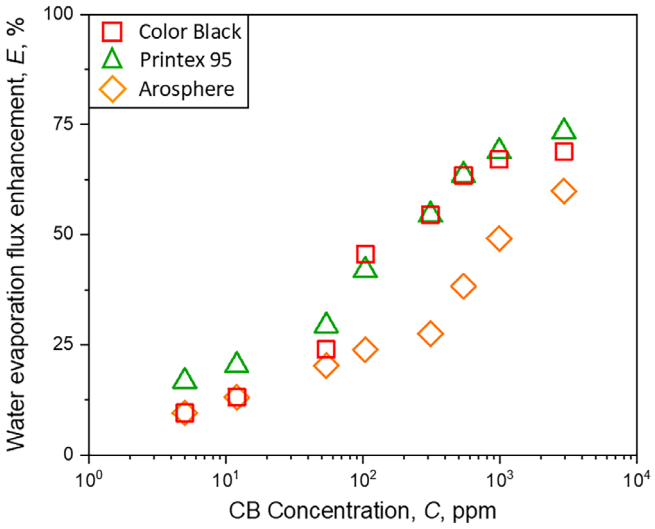

FIGURE 7 Water evaporation flux enhancement, *E*, as a function of CB concentration, *C*, measured in water solutions containing Color Black (squares), Printex 95 (triangles), and Arosphere (diamonds).

4 | CONCLUSIONS

In this work, a detailed physicochemical characterization of commercial carbon black (CB) grades was presented to determine the

link between various particle properties and the performance of CB in solar steam generation, for the first time to the best of our knowledge. The CB nanoparticles used here have surface mean primary particle diameters, $d_{va} = 11–406$ nm and specific surface area, $SSA = 8–300$ m^2/g. Thermogravimetric analysis, Raman spectroscopy and x-ray diffraction reveal that fine CB nanoparticles (Color Black and Printex 95) with $d_{va} = 11–14$ nm have a more disordered structure and larger organic carbon content than coarse CB grades (Printex U, Printex G, Lamp Black, and Arosphere) with $d_{va} = 38–406$ nm. Most importantly, UV–vis spectroscopy shows that increasing the particle d_{va} from 14 to 406 nm reduces the light absorption of CB dispersed in water up to 86% and weakens its dependence on wavelength. Mie theory calculations with constant and variable refractive indexes show that increasing particle size reduces the CB *MAC*, while variations of the particle nanostructure and OC content hardly affect it. So, the particle size determines the CB light absorption and affects the solar steam generation by aqueous CB suspensions. In particular, the water evaporation flux measured here for suspensions containing CB nanoparticles with $d_{va} = 11–14$ nm is up to 25% larger than that obtained for suspensions of coarse CB with $d_{va} = 406$ nm. In sum, the performance of CB in solar steam generation is determined by its light absorption quantified by *MAC* that is affected mostly by the particle size. Thus, good control of particle size is essential to optimize the solar steam generation enabled by CB.

AUTHOR CONTRIBUTIONS

Georgios A. Kelesidis: Conceptualization; methodology; supervision; visualization; writing – original draft; writing – review and editing; formal analysis. **Amogh Nagarkar:** Methodology; writing – review and editing; formal analysis; investigation. **Pier Giuseppe Rivano:** Software; methodology; investigation; writing – review and editing; formal analysis.

ACKNOWLEDGMENTS

This research was funded by the Particle Technology Laboratory, ETH Zurich and by Swiss National Science Foundation (200020_182668, 250320_163243, and 206021_170729). We gratefully acknowledge the support of Dr. K. Rockstein (Orion Engineered Carbons) for providing the CB grades, Dr. F. Krumeich for microscopy imaging, and Prof. S. E. Pratsinis for stimulating discussions. Open access funding provided by Eidgenossische Technische Hochschule Zurich.

DATA AVAILABILITY STATEMENT

The numerical data from Figures 2–7 and S1–S3 are tabulated in a .xlsx file in the Supporting Information.

ORCID

Georgios A. Kelesidis https://orcid.org/0000-0003-4220-9649
Pier Giuseppe Rivano https://orcid.org/0009-0005-9568-7291

REFERENCES

1. Mills D. Advances in solar thermal electricity technology. *Sol Energy*. 2004;76:19-31.
2. Zhou L, Tan YL, Wang JY, et al. 3D self-assembly of aluminium nanoparticles for plasmon-enhanced solar desalination. *Nat Photonics*. 2016;10:393-398.
3. Neumann O, Feronti C, Neumann AD, et al. Compact solar autoclave based on steam generation using broadband light-harvesting nanoparticles. *PNAS*. 2013;110:11677-11681.
4. Jin HC, Lin GP, Bai LZ, Zeiny A, Wen DS. Steam generation in a nanoparticle-based solar receiver. *Nano Energy*. 2016;28:397-406.
5. Wang XZ, He YR, Liu X, Shi L, Zhu JQ. Investigation of photothermal heating enabled by plasmonic nanofluids for direct solar steam generation. *Sol Energy*. 2017;157:35-46.
6. Elimelech M, Phillip WA. The future of seawater desalination: energy, technology, and the environment. *Science*. 2011;333:712-717.
7. Sharon H, Reddy KS. A review of solar energy driven desalination technologies. *Renew Sustain Energy Rev*. 2015;41:1080-1118.
8. Xiao G, Wang XH, Ni MJ, et al. A review on solar stills for brine desalination. *Appl Energy*. 2013;103:642-652.
9. Orrett FA, Brooks PJ, Richardson EG. Nosocomial infections in a rural regional hospital in a developing country: infection rates by site, service, cost, and infection control practices. *Infect Control Hosp Epidemiol*. 1998;19:136-140.
10. Ni G, Miljkovic N, Ghasemi H, et al. Volumetric solar heating of nanofluids for direct vapor generation. *Nano Energy*. 2015;17:290-301.
11. Halas NJ, Lal S, Chang WS, Link S, Nordlander P. Plasmons in strongly coupled metallic nanostructures. *Chem Rev*. 2011;111:3913-3961.
12. Zhao DW, Duan HZ, Yu ST, et al. Enhancing localized evaporation through separated light absorbing centers and scattering centers. *Sci Rep*. 2015;5:17276.
13. Wegner K, Pratsinis SE. Scale-up of nanoparticle synthesis in diffusion flame reactors. *Chem Eng Sci*. 2003;58:4581-4589.
14. Zeiny A, Jin HC, Lin GP, Song PX, Wen DS. Solar evaporation via nanofluids: a comparative study. *Renew Energy*. 2018;122:443-454.
15. Khodabakhshi S, Fulvio PF, Andreoli E. Carbon black reborn: structure and chemistry for renewable energy harnessing. *Carbon*. 2020;162:604-649.
16. Kelesidis GA, Goudeli E, Pratsinis SE. Morphology and mobility diameter of carbonaceous aerosols during agglomeration and surface growth. *Carbon*. 2017;121:527-535.
17. Kelesidis GA, Benz S, Pratsinis SE. Process design for carbon black size and morphology. *Carbon*. 2023;213:118255.
18. Lahaye J, Ehrburgerdolle F. Mechanisms of carbon-black formation—correlation with the morphology of aggregates. *Carbon*. 1994;32:1319-1324.
19. Monthioux M. Describing carbons. *Carbon Trends*. 2024;14:100325.
20. Lapuerta M, Oliva F, Agudelo JR, Stitt JP. Optimization of Raman spectroscopy parameters for characterizing soot from different diesel fuels. *Combust Sci Technol*. 2011;183:1203-1220.
21. Iwashita N, Park CR, Fujimoto H, Shiraishi M, Inagaki M. Specification for a standard procedure of x-ray diffraction measurements on carbon materials. *Carbon*. 2004;42:701-714.
22. Lim S, Lee S, Ahn T, Park S. Measurement of organic carbon content during the growth of soot particles in propane normal and inverse diffusion flames using a multi-wavelength light extinction method. *Carbon*. 2019;149:519-529.
23. Trivanovic U, Martins MP, Benz S, Kelesidis GA, Pratsinis SE. Dynamics of soot surface growth and agglomeration by enclosed spray combustion of jet fuel. *Fuel*. 2023;342:127864.
24. Trivanovic U, Kelesidis GA, Pratsinis SE. High-throughput generation of aircraft-like soot. *Aerosol Sci Tech*. 2022;56:732-743.
25. Liu CR, Singh AV, Saggese C, et al. Flame-formed carbon nanoparticles exhibit quantum dot behaviors. *PNAS*. 2019;116:12692-12697.

26. Kelesidis GA, Bruun CA, Pratsinis SE. The impact of organic carbon on soot light absorption. *Carbon*. 2021;172:742-749.
27. Kelesidis GA, Pratsinis SE. Soot light absorption and refractive index during agglomeration and surface growth. *Proc Combust Inst*. 2019; 37:1177-1184.
28. Neumann O, Urban AS, Day J, Lal S, Nordlander P, Halas NJ. Solar vapor generation enabled by nanoparticles. *ACS Nano*. 2013;7:42-49.
29. Dongare PD, Alabastri A, Pedersen S, et al. Nanophotonics-enabled solar membrane distillation for off-grid water purification. *PNAS*. 2017;114:6936-6941.
30. Orion Engineered Carbons. Accessed September 28, 2024. https://orioncarbons.com/wp-content/uploads/2023/04/22_06_21_td_0112_farbrusstabelle_emea_web_2.pdf
31. Kruk M, Jaroniec M. Gas adsorption characterization of ordered organic–inorganic nanocomposite materials. *Chem Mater*. 2001;13: 3169-3183.
32. Eggersdorfer ML, Gröhn AJ, Sorensen CM, McMurry PH, Pratsinis SE. Mass-mobility characterization of flame-made ZrO_2 aerosols: primary particle diameter and extent of aggregation. *J Colloid Interf Sci*. 2012; 387:12-23.
33. Lapuerta M, Oliva F, Agudelo JR, Boehman AL. Effect of fuel on the soot nanostructure and consequences on loading and regeneration of diesel particulate filters. *Combust Flame*. 2012;159:844-853.
34. Sadezky A, Muckenhuber H, Grothe H, Niessner R, Pöschl U. Raman microspectroscopy of soot and related carbonaceous materials: spectral analysis and structural information. *Carbon*. 2005;43:1731-1742.
35. Baldelli A, Rogak SN. Morphology and Raman spectra of aerodynamically classified soot samples. *Atmos Meas Technol*. 2019;12:4339-4346.
36. Ferrari AC, Robertson J. Resonant Raman spectroscopy of disordered, amorphous, and diamondlike carbon. *Phys Rev B*. 2001;64: 075414.
37. Klingshirn CD, West ZJ, DeWitt MJ, Higgins A, Graham J, Corporan E. Quantification of elemental and total carbon in combustion particulate matter using thermal-oxidative analysis. *J Air Waste Manage Assoc*. 2019;69:1003-1013.
38. Dastanpour R, Rogak SN. The effect of primary particle polydispersity on the morphology and mobility diameter of the fractal agglomerates in different flow regimes. *J Aerosol Sci*. 2016;94:22-32.
39. Wiscombe WJ. Improved Mie scattering algorithms. *Appl Opt*. 1980; 19:1505-1509.
40. Yon J, Bescond A, Liu F. On the radiative properties of soot aggregates. Part 1: necking and overlapping. *J Quant Spectrosc Radiat Transf*. 2015;162:197-206.
41. Kelesidis GA, Neubauer D, Fan LS, Lohmann U, Pratsinis SE. Enhanced light absorption and radiative forcing by black carbon agglomerates. *Environ Sci Technol*. 2022;56:8610-8618.
42. Kelesidis GA, Kholghy MR, Zuercher J, et al. Light scattering from nanoparticle agglomerates. *Powder Technol*. 2020;365:52-59.
43. Kelesidis GA, Crepaldi P, Allemann M, Duric A, Pratsinis SE. The mobility diameter of soot determines its angular light scattering distribution. *Combust Flame*. 2023;258:112476.
44. Kelesidis GA, Gao D, Starsich FHL, Pratsinis SE. Light extinction by agglomerates of gold nanoparticles: a plasmon ruler for sub-10 nm interparticle distances. *Anal Chem*. 2022;94:5310-5316.
45. Kelesidis GA, Goudeli E, Pratsinis SE. Flame synthesis of functional nanostructured materials and devices: surface growth and aggregation. *Proc Combust Inst*. 2017;36:29-50.
46. Draine BT, Flatau PJ. Discrete-dipole approximation for scattering calculations. *J Opt Soc Am A*. 1994;11:1491-1499.
47. Doner N, Liu FS. Impact of morphology on the radiative properties of fractal soot aggregates. *J Quant Spectrosc Radiat Transf*. 2017;187:10-19.
48. Pahalagedara L, Sharma H, Kuo CH, et al. Structure and oxidation activity correlations for carbon blacks and diesel soot. *Energy Fuel*. 2012;26:6757-6764.
49. Moore RH, Ziemba LD, Dutcher D, et al. Mapping the operation of the miniature combustion aerosol standard (Mini-CAST) soot generator. *Aerosol Sci Tech*. 2014;48:467-479.
50. Kelesidis GA, Rossi N, Pratsinis SE. Porosity and crystallinity dynamics of carbon black during internal and surface oxidation. *Carbon*. 2022; 197:334-340.
51. Kelesidis GA, Nagarkar A, Trivanovic U, Pratsinis SE. Toward elimination of soot emissions from jet fuel combustion. *Environ Sci Technol*. 2023;57:10276-10283.
52. De Falco G, Commodo M, Bonavolontà C, Pepe GP, Minutolo P, D'Anna A. Optical and electrical characterization of carbon nanoparticles produced in laminar premixed flames. *Combust Flame*. 2014;161: 3201-3210.
53. Dastanpour R, Momenimovahed A, Thomson K, Olfert J, Rogak S. Variation of the optical properties of soot as a function of particle mass. *Carbon*. 2017;124:201-211.
54. Zangmeister CD, You R, Lunny EM, et al. Measured mass absorption spectra for nine forms of highly-absorbing carbonaceous aerosol. *Carbon*. 2018;136:85-93.

SUPPORTING INFORMATION

Additional supporting information can be found online in the Supporting Information section at the end of this article.

How to cite this article: Kelesidis GA, Nagarkar A, Rivano PG. Solar steam generation enabled by carbon black: The impact of particle size and nanostructure. *AIChE J*. 2024;e18619. doi:10.1002/aic.18619